https://doi.org/10.5194/egusphere-2026-3987
Preprint. Discussion started: 28 July 2026

How do clouds and turbulence shape the northeasterly low-level jet of a summertime Arctic cyclone during its cold core transition ?

Nicolas Chiabrando[1], Gwendal Rivière[1], Étienne Vignon[1], and Julien Delanoë[2]

[1]Laboratoire de Météorologie Dynamique-IPSL, Sorbonne Université/CNRS/ Ecole Normale Supérieure-PSL Université/ Ecole Polytechnique-Institut Polytechnique de Paris, Paris, France
[2]LATMOS, Observatoire de Versailles Saint-Quentin-en-Yvelines (OVSQ), Université Paris-Saclay, UVSQ, CNRS, Guyancourt, France

Correspondence: Nicolas Chiabrando (nicolas.chiabrando@lmd.ipsl.fr)

Abstract. Synoptic-scale Arctic cyclones play a major role in the polar climate variability by bringing heat and humidity from lower latitudes. However, they have not been as intensively studied as mid-latitudes cyclones, and some questions about their development processes remain unresolved. The international THINICE campaign which occurred in August 2022 near Svalbard archipelago aimed at studying Arctic cyclones and in particular low-level jets (LLJs) along fronts that can favour sea ice breakup and contribute the heat and moisture meridional atmospheric transport. By comparing ERA5 reanalysis with radar observations from the campaign, we show that ERA5 reasonably captures the LLJs correctly, in particular several cold-conveyor-belt (CCB) jets, but tends to slightly underestimate their intensity and to position them not close enough to the surface. It is therefore essential to understand the processes that drive the structure and intensity of these LLJs among which diabatic and frictional processes associated with clouds and turbulence that is, processes that are fully parameterised in numerical weather prediction and climate models. The objective of the present work is to understand how clouds and turbulence shape an intense LLJ during the typical warm-core to cold-core transition of a well-observed Arctic cyclone during THINICE. The analysis is conducted using the ERA5 analyses and short-term forecasts. It is based on the computation of backward Lagrangian trajectories initialised in a narrow band of high potential vorticity (PV) associated with the northeasterly LLJ. A PV budget is performed in which all the diabatic - mostly associated with cloud condensation and radiative effects - and frictional PV tendency terms are computed and investigated. Results show that both diabatic and frictional terms reinforce the potential vorticity gradient across the jet and therefore its intensity when the system is baroclinic. Under such a baroclinic growth phase, the northeasterly LLJ is well identified as a CCB jet along the bent-back warm front. However, when the system is not baroclinic anymore and reaches a cold-core structure, friction generates much less PV and has almost no effect. Radiative cooling above boundary layer clouds no longer generates PV either, unlike during the baroclinic phase, and even slightly destroys it. Heating from condensation inside thick frontal clouds generate the same amount of PV in both phases (baroclinic and cold-core phases). Overall there is less PV generation in the second phase than in the first phase, which overall leads to a less intense LLJ.

https://doi.org/10.5194/egusphere-2026-3987
Preprint. Discussion started: 28 July 2026

1 Introduction

Arctic cyclones correspond to synoptic-scale depressions that travel inside the Arctic circle. They differ from the polar lows that are intense maritime meso-scale cyclones travelling at high latitudes (Stoll et al., 2018). They are a key component of the rapidly changing Arctic climate (Serreze et al., 2009) as they transport humidity and heat from mid-latitudes to the pole. They are also the main contributors to weather variability in the Arctic by forming strong surface winds and precipitation, impacting local populations and human activities in that part of the world (Waseda et al., 2021). Interactions between Arctic cyclones and sea ice is also an important debated topic, especially in summer when sea ice is melting (Finocchio et al., 2022; Peng et al., 2021; Screen et al., 2011). Arctic cyclones exhibit a marked seasonal variability, with more cyclones but less intense cyclones in summer than in winter (Zhang et al., 2004). Summertime cyclones also have a longer lifespan than in winter and than mid-latitude winter cyclones on average (Vessey et al., 2022). A particular feature of those cyclones is that they can have a low-level dominant structure associated with a warm core, similar to mid-latitude cyclones, or an upper-level dominant one associated with a cold core (Croad et al., 2023b). The long Arctic cyclones usually transition from a warm core structure toward a cold core just after they reach their maximum deepening (Besson et al., 2026a). The cold-core structure (Croad et al., 2023a) and the absence of occlusion (Vessey et al., 2022) have been suggested to explain the longer lifespan of Arctic cyclones compared to mid-latitude ones. They are initiated by baroclinic growth or Lee cyclogenesis, similarly to mid-latitude cyclones, and many of them grow through the interaction with tropopause polar vortices (Gray et al., 2021). They can be initiated in the Arctic or in mid-latitudes and then transition towards the Arctic where they can move with complex trajectories as there is no dominant wind (Tanaka et al., 2012).

The international airborne campaign THINICE organised in summer 2022 (Rivière et al., 2024) was the first campaign specifically dedicated to the study of summer time Arctic cyclones, and their interaction with sea ice and tropopause polar vortices. The campaign sampled many low-level jets (LLJ) along the fronts of Arctic cyclones. Such jets are key features of the Arctic climate as they can interact with the surface, with the turbulent boundary layer and sea ice. During the THINICE campaign, the most often observed LLJs were Cold Conveyor Belt (CCB) jets which correspond to airflows on the cold side of warm fronts (Carlson, 1980; Schultz, 2001). The CCB jet mainly turns cyclonically poleward of the low pressure center and brings cold air equatorward upstream of the low pressure centre. In some observed cases, it is difficult to attribute the LLJ to a well defined classical air mass of mid-latitude conceptual models as Arctic cyclones have their own specificities. That was particularly the case of the cyclone hereafter studied that transitioned from a baroclinic structure to a cold-core barotropic structure.

A body of litterature have shown the importance of cloud processes and boundary-layer turbulence in the intensity of the extra-tropical cyclones, and in particular in the intensity of LLJs (Wernli and Gray, 2024). A common methodology used to study those mechanisms is the Ertel Potential Vorticity (PV) framework which is a conserved quantity in absence of frictional and diabatic processes (Ertell, 1942). PV is thus useful to investigate the impact of non conserved processes on cyclone dynamics (Stoelinga, 1996; Adamson et al., 2006). Attinger et al. (2019) performed a PV budget on a case study of a spring North Pacific cyclone. Using a Lagrangian approach, they found out that the PV band along the warm front, directly related

https://doi.org/10.5194/egusphere-2026-3987
Preprint. Discussion started: 28 July 2026

with the CCB, is mostly generated by a combination of condensation processes, turbulence and long-wave radiative cooling. Attinger et al. (2021) applied the same methodology on a set of 288 extratropical cyclones and they further show that turbulent mixing of momentum is in fact the main process generating low-level PV at the warm front during summer and by condensation during winter. However, they also observed large case-to-case and seasonal variability.

Only a limited number of studies have analysed Arctic cyclones within the PV framework. Croad et al. (2023a) showed how boundary-layer processes generated PV in two distinct summertime Arctic cyclones. One cyclone had a warm core where the vorticity was dominated by the low levels, and the other had a cold core and dominated by upper levels. By performing an integrated PV budget over the whole boundary-layer, they showed that the main difference between the two cyclones is the baroclinic generation of PV associated with friction, which acts differently depending on the cyclone structure. Indeed, this term generates PV when surface wind is opposite to thermal wind and destroys PV if they are oriented in the same direction (Cooper et al., 1992; Adamson et al., 2006). During baroclinic growth, this term generates one order of magnitude more PV in the warm-core cyclone than in the cold-core one. After maximum intensity, the same process is slightly destroying low-level PV in both cyclones, making the lower-level dominant cyclone transitioning toward an upper-level dominant structure after a few days and reinforcing the upper-level structure in the cold-core one. It has been suggested that such findings might explain the particular long lifespan of cold-core Arctic cyclones compared to warm-core cyclones. However, this study did not consider the effects of clouds through their radiative and latent effects, and only studied the effects of friction and sensible heat fluxes on the boundary-layer PV budget.

The aim of this study is to investigate the roles of diabatic and frictional processes associated with clouds and turbulence in shaping the northwesterly LLJ of an intensively observed Arctic cyclone during THINICE when transitioning from a baroclinic structure to a cold-core axisymmetric structure. During the baroclinic phase, the studied northwesterly LLJ resembles the CCB jet of a typical mid-latitude cyclone but then, during the transition toward the axisymmetric structure, the warm front becomes less and less active and the LLJ lost part of its properties. Our study uses observations from the campaign and performs a PV budget using a Lagrangian trajectory algorithm applied to ERA5 reanalysis and short-term forecasts. We quantify the respective contributions processes of clouds and friction on the formation, maintenance and decay of this CCB LLJ, and analyse the differences between the two phases of the cyclone life.

The paper is structured as follows. Section 2 starts by introducing the ERA5 data, the THINICE observations and the methodology, namely the PV framework and the Lagrangian backward trajectory algorithm. Section 3 gives an overall description of the cyclone case study and presents observations of the associated CCB. It also assesses the representation of other LLJs of the THINICE campaign in ERA5 by comparing with airborne observations. Section 4 presents the results of the study of the links between fine-scale processes and the northeasterly LLJ. Results are synthesised and discussed in Section 5.

https://doi.org/10.5194/egusphere-2026-3987
Preprint. Discussion started: 28 July 2026

2 Data and methods

2.1 ERA5 reanalyses and short-term forecasts

We use the ERA5 (Hersbach et al., 2020) reanalysis and short-term forecasts from the European Centre for Medium Range Weather Forecasts (ECMWF) with a $0.25° \times 0.25°$ hourly grid. Forecasts are initialised twice daily with the analyses at 06 UTC and 18 UTC and last 18 hours. Some variables are only available from the forecasts such as the momentum and temperature tendencies from physical parameterisations and this is the reason why the forecasts outputs are systematically used in the present study. In particular we have access to the temperature tendencies due to long-wave and short-wave radiative effects and to the total temperature tendencies from all parameterisations. The latter includes latent heating or cooling from water phase changes, radiative effects, turbulent vertical heat transport, cloud parameterisation, convection (ECMWF, 2026)... The total momentum tendencies due to subgrid parameterisation of turbulent diffusion and gravity wave drag are also available but are not decomposed into distinct processes. The tendencies due to parameterisations are given as hourly time-averages while other forecasts outputs such as the wind or the temperature are instantaneous. Additionally, since the temperature tendencies are equal to zero at the initial time of the forecasts, we use the lead time of the forecasts between +1h to +12h. Thus for UTC hours between 19:00 at day D0 and 06:00 UTC at day D0+1, we use the forecast initialised at 18:00 UTC at day D0. For UTC hours between 07:00 and 18:00 we use the forecast initialised at 06:00 UTC the same day. The use of different short-term forecasts may lead to potential discontinuities between 06:00 UTC and 07:00 UTC or between 18:00 UTC and 19:00 UTC but these are negligible.

All the variables of the short-term forecasts are made available on the 137 model levels. We have interpolated them onto isobaric surfaces every 10hPa close to the surface (between 1000 hPa and 700hPa and every 50 hPa between 700 hPa and 100 hPa) to show horizontal maps at a given pressure level and vertical cross sections with the pressure as the vertical coordinate.

2.2 Radar wind-speed observation during THINICE

The international airborne field campaign THINICE organised in summer 2022 in Svalbard investigated the dynamics of Arctic cyclones and tropopause polar vortices and their interactions with cloud microphysics, sea surface and sea ice (Rivière et al., 2024). It involved two instrumented research aircraft: the Twin Otter from the British Antarctic Survey and the ATR42 from SAFIRE (the French facility for airborne research). The latter was equipped, amongst other instruments, with a 95-GHz Doppler cloud radar named RASTA (Delanoë et al., 2013). In addition to the reflectivity, and thanks to the three antennas pointing upward and the three antennas pointing downward, the 3D components of the wind are retrieved in cloudy regions over the whole troposphere along the aircraft path. We combine the RASTA wind measurements with in-situ aircraft wind measurements. The difference between in-situ wind speed measurements from the aircraft and the RASTA measurements 300 m below the aircraft has a small mean of 0.17 m/s and a standard deviation of 2.2 m/s when computed over all the flights conducted during RALI-THINICE (not shown).

https://doi.org/10.5194/egusphere-2026-3987
Preprint. Discussion started: 28 July 2026

2.3 Potential Vorticity

The potential vorticity (PV) framework is hereafter adopted to study non conservative processes influencing the LLJ. The Ertel PV and its Lagrangian derivative are defined as:

$$q = \frac{1}{\rho}\boldsymbol{\zeta_a}.\boldsymbol{\nabla}\theta, \tag{1}$$

$$\frac{Dq}{Dt} = \frac{1}{\rho}(\boldsymbol{\zeta_a}.\boldsymbol{\nabla}\dot{\theta} + \boldsymbol{\nabla}\times\boldsymbol{F}.\boldsymbol{\nabla}\theta), \tag{2}$$

where $\boldsymbol{\zeta_a}$ is the 3D absolute vorticity vector, ρ the air density, θ the potential temperature and $\boldsymbol{F}$ the three-dimensional frictional acceleration. The Lagrangian derivative of the potential temperature is defined as $\dot{\theta} = \frac{D\theta}{Dt}$ and $\boldsymbol{\nabla}$ is the three dimensional vector gradient. One can already notice that if there is no friction nor temperature changes, PV is conserved. In pressure coordinates, those equations can be rewritten as:

$$q = -g\left[(\zeta+f)\frac{\partial\theta}{\partial p} + \frac{\partial u}{\partial p}\frac{\partial\theta}{\partial y} - \frac{\partial v}{\partial p}\frac{\partial\theta}{\partial x}\right], \tag{3}$$

$$\frac{Dq}{Dt} = -g\Big[\underbrace{(\zeta+f)\frac{\partial\dot{\theta}}{\partial p} + \frac{\partial u}{\partial p}\frac{\partial\dot{\theta}}{\partial y} - \frac{\partial v}{\partial p}\frac{\partial\dot{\theta}}{\partial x}}_{\text{Diabatic terms}} + \underbrace{\overbrace{(\frac{\partial F_y}{\partial x} - \frac{\partial F_x}{\partial y})\frac{\partial\theta}{\partial p}}^{\text{Ekman term}} + \overbrace{\frac{\partial F_x}{\partial p}\frac{\partial\theta}{\partial y} - \frac{\partial F_y}{\partial p}\frac{\partial\theta}{\partial x}}^{\text{Baroclinic term}}}_{\text{Frictional terms}}\Big], \tag{4}$$

with F_x, F_y and u, v being the horizontal components of $\boldsymbol{F}$ and wind vector respectively, f the Coriolis parameter and ζ the vertical component of the relative vorticity. The first three terms on the right-hand side of Eq. (4) can be seen as the diabatic generation of PV as they include $\dot{\theta}$. In ERA5 short-term forecasts, we have access to the total temperature tendencies due to long-wave and short-wave radiative effects. We can then decompose the diabatic generation of PV between its radiative contribution and the non-radiative contribution. Similarly, the last three terms can be viewed as the frictional generation of PV because they include the horizontal components of the wind drag vector $\boldsymbol{F}$. As in Croad et al. (2023a), the first of those three term is named the Ekman term and the two other are referred to as the baroclinic frictional generation term as they include the horizontal components of the temperature gradients. A summary of this decomposition is shown in Tab. 1. The different terms are computed by applying finite-difference schemes to the variables F_x, F_y, u, v and $\dot{\theta}$ on a $0.25° \times 0.25°$ horizontal grid and 10-hPa evenly spaced vertical levels.

2.4 Lagrangian tracking algorithm

In order to understand where and how the PV is generated, a PV budget along air parcel backward-trajectories is performed using the Lagrantraj Lagrangian tracking algorithm described in Rivière et al. (2021) and already used in several studies (Wimmer et al., 2022; Deshmukh et al., 2025). Trajectories are initialised from high-PV, that are regions where the PV is above 2 PVU, every 10 hPa between 950hPa and 850 hPa and every 0.25° of latitude and 1° of longitude along the PV band associated with the studied LLJ.

https://doi.org/10.5194/egusphere-2026-3987
Preprint. Discussion started: 28 July 2026

Table 1. Summary of non conserved processes considered in this study. The first row shows the abbreviation of the corresponding accumulated PV, the second row a description of the process and the third row the corresponding physical process.

Abbreviation	Description	Physical processes
$\Delta PV_{friction}$	Sum of all wind tendencies due to parameterisations, i.e. convection, turbulence and gravity wave drag	$\boldsymbol{F}$
$\Delta PV_{heating}$	Sum of all temperature tendencies due to parameterisations, i.e. large-scale microphysics, radiative processes, convection, turbulence and gravity wave drag	$\dot{\theta}$ (total)
ΔPV_{rad}	Sum of temperature tendencies due to the parameterisations of short-wave and long-wave radiative effects	$\dot{\theta}_{SW} + \dot{\theta}_{LW}$
$\Delta PV_{heating-rad}$	Sum of all temperature tendencies due to parameterisations except radiative processes	$\dot{\theta} - \dot{\theta}_{SW} - \dot{\theta}_{LW}$

3 Cyclone AC3: representation in THINICE observations and ERA5 reanalysis

In this study, we choose to focus on the third cyclone observed during the campaign, that will be referred to as AC3 in the following. This cyclone experiences a transition from a baroclinic structure and neutral core temperature toward a cold-core axisymmetric structure, as we can observe in Fig. 1c. This figure shows the difference between the mean temperature inside a circle of radius 100 km around the cyclone pressure centre and the mean temperature around the cyclone on a 1000km radius circle (similarly as in Besson et al. (2026a)). The trajectory of the cyclone and the mean sea ice concentration during August 2022 are shown in Fig. 1a. AC3 is formed on the South East coast of Greenland on 13 August 2022. Its transition toward a cold-core structure starts around 16 August and ends around 20 August. During this transition, it reaches a sea level pressure minimum of 990 hPa on 18 August (Fig. 1b). It reaches sea ice roughly at the same time. After the 20th of August, the cyclone moves with a more chaotic trajectory near the pole before decaying over northern Siberia.

Six flights of the ATR42 aircraft have been conducted over AC3. In particular, the northeasterly LLJ north of the cyclone center has been crossed two times during flights F46 and F49. Flight 46 occurred from 12:30 to 16:50 UTC on 16 August and crossed the cyclone during its growth phase and at the beginning of its transition toward the cold-core structure. Its trajectory can be seen in the left panel of Fig. 2 which shows the wind and the potential temperature of the cyclone at 14:00 UTC on 16 August at 950 hPa. At that time, the cold front is along the Norwegian coastline and perpendicular to the zonally-oriented warm front. During F46, the ATR42 aircraft crossed the warm front several times at different levels and the associated jet on its cold side which can be therefore identified as a CCB jet. In the right panels, is shown a comparison of the horizontal wind speed of the LLJ observed along flight 46 by the RASTA radar with ERA5 short-term forecasts. We can see that ERA5 forecasts qualitatively capture the CCB jet but slightly underestimates its intensity and positions the jet more to the north compared to the observations.

https://doi.org/10.5194/egusphere-2026-3987
Preprint. Discussion started: 28 July 2026

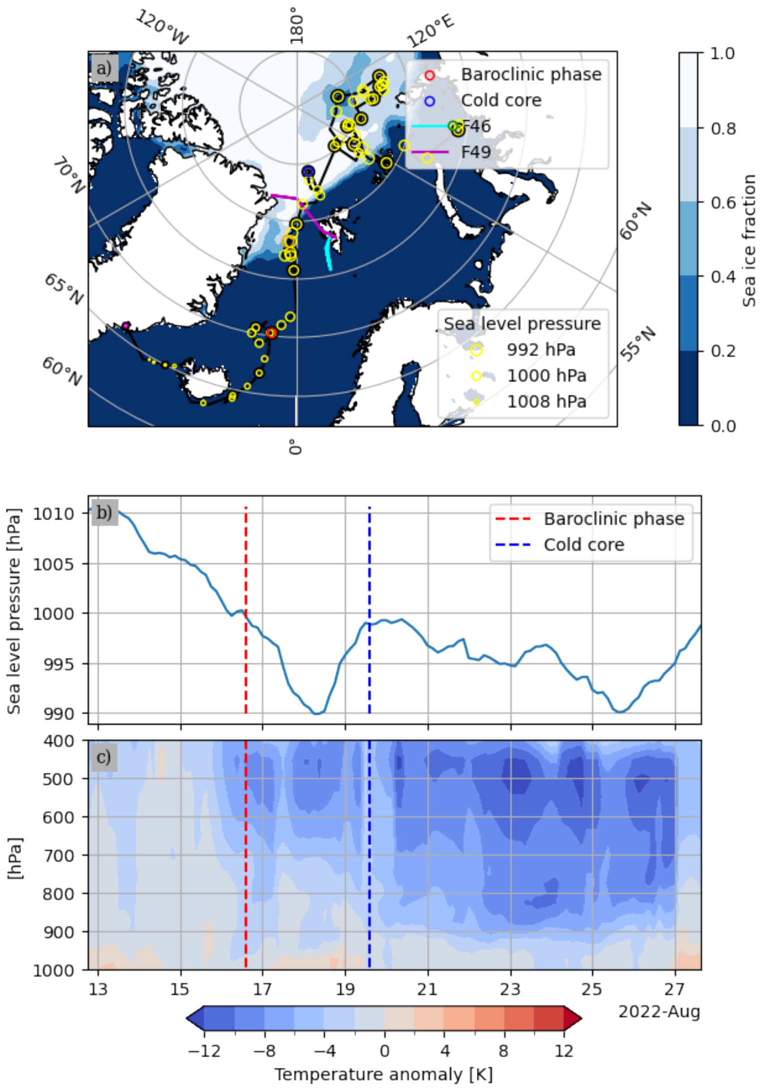

Figure 1. Description of cyclone AC3. *a)* Mean sea ice concentration during August 2022 and cyclone trajectory. Each yellow point is the position of the cyclone pressure centre every 6 hours. Their size is proportional to the sea level pressure. Those with a black edge are every 24 hours. Orange circles correspond to times when the cyclone is the deepest. The beginning and the end of the trajectory are indicated in purple and green respectively. *b)* Evolution of sea level pressure at the cyclone pressure centre. *c)* Temperature anomaly of the cyclone centre. It is computed as the difference between the mean temperature inside a 100km radius circle around the cyclone low pressure centre and the mean temperature on a 1000km radius circle around the cyclone centre with a width of 100km. Positions and dates of the baroclinic phase and cold core phase are indicated. Data are from ERA5 reanalysis. The trajectory is obtained using an algorithm tracking the sea level pressure minimum, described in Besson et al. (2026a).

https://doi.org/10.5194/egusphere-2026-3987
Preprint. Discussion started: 28 July 2026

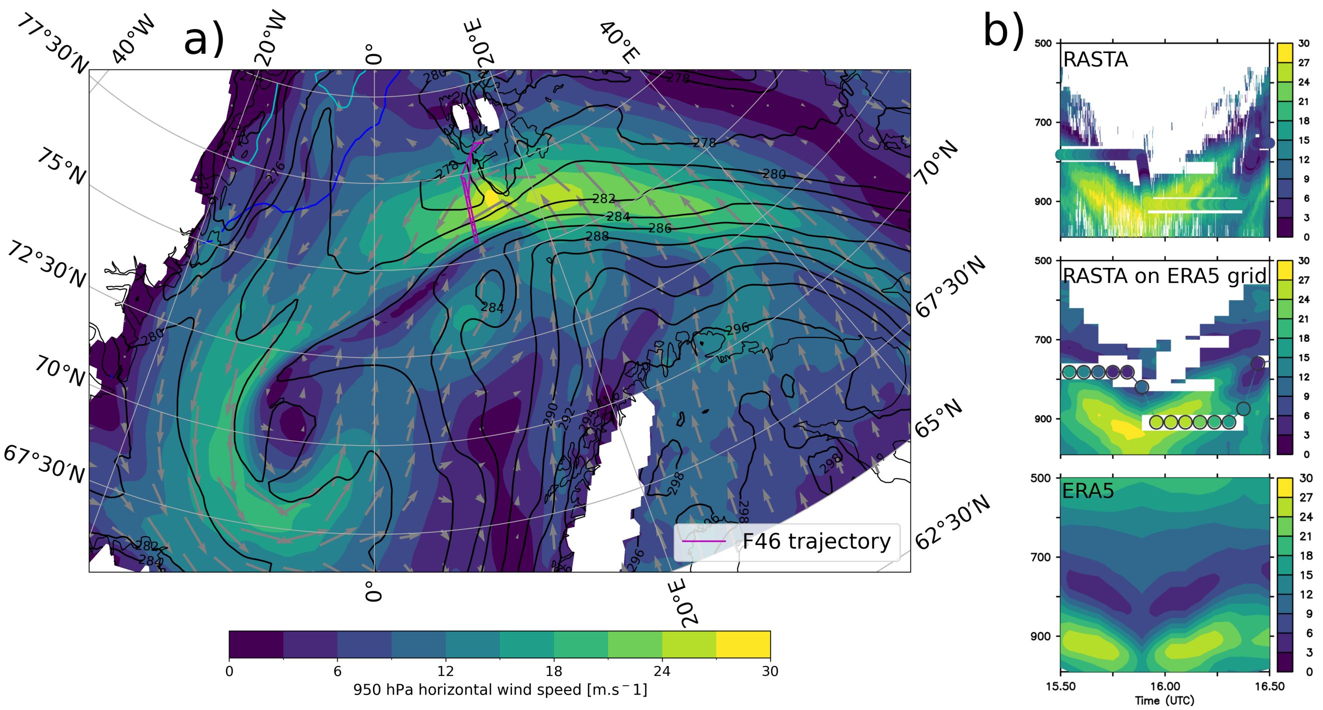

Figure 2. General structure of cyclone AC3 during its baroclinic phase at 14:00 UTC on 16 August. *(a)* Wind speed (shading) and its directions (grey arrows) and potential temperature (black contours) at 950 hPa. The trajectory of the ATR42 during the flight F46 of the THINICE campaign is shown in magenta line. Cyan contour and dark blue lines correspond to, respectively, the 0.8 and 0.2 sea ice fractions. **(b)** Observed horizontal wind speed of the CCB along the flight 46 by the RASTA radar (upper panel), interpolated on the ERA5 short-term forecasts grid (middle panel) compared with ERA5 short-term forecast (lower panel). The ERA5 short-term forecast is initialised at 06 UTC on 16 August. The circles on the RASTA plots correspond to aircraft in-situ wind measurements.

A similar analysis is plotted in Fig. 3 with flight F49 which was conducted from 12:00 to 16:20 UTC on 19 August and crossed the cyclone during the end of its transition toward cold core. ERA5 forecasts simulate the LLJ at the correct location but still underestimates its intensity (Fig. 3b). The LLJ is also a northeasterly jet as for flight F46 but the warm front is not visible anymore and the associated jet can hardly be considered as a CCB jet.

The present study focuses on those two periods of the cyclone life cycle corresponding to flights F46 and F49 because they represent the beginning and the end of the typical transition phase undergone by many summertime Arctic cyclones: moving from the growing phase characterised by a baroclinic structure, well-defined fronts and a neutral core temperature at 14:00 on 16 August, to the beginning of the cold-core phase at 14:00 on 19 August (Fig. 1b,c).

https://doi.org/10.5194/egusphere-2026-3987
Preprint. Discussion started: 28 July 2026

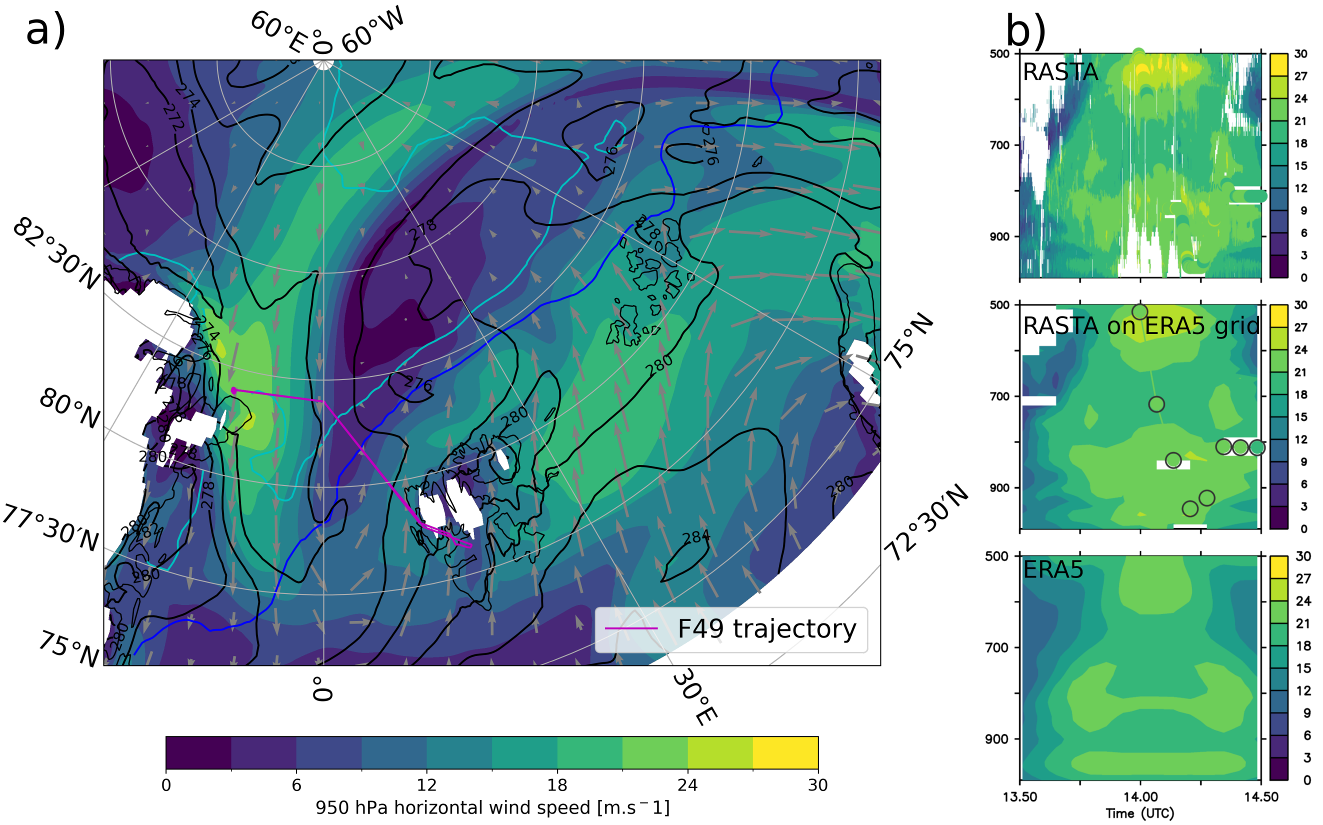

Figure 3. General structure of cyclone AC3 during the beginning of the cold-core phase at 14:00 UTC on 19 August. *(a)* Wind speed (colorbar) and its directions (grey arrows) and potential temperature (black contours) at 950 hPa. The trajectory of the ATR42 during the flight F49 of the THINICE campaign is shown in magenta line. Cyan contour and dark blue lines correspond to, respectively, the 0.8 and 0.2 sea ice fractions. **(b)** Observed horizontal wind speed of the CCB along the flight 46 by the RASTA radar (upper panel), interpolated on the ERA5 short-term forecasts grid (middle panel) compared with ERA5 short-term forecast (lower panel). The ERA5 short-term forecast is initialised at 06 UTC on 19 August. The circles on the RASTA plots correspond to aircraft in-situ wind measurements.

3.1 Other observations of LLJs during THINICE

During THINICE, 16 flights of the SAFIRE ATR42 aircraft have been conducted to sample various components of Arctic cyclones and 11 flights among them observed a LLJ (Rivière et al., 2024). Figure 4 compares radar airborne observations of LLJs with ERA5 short-term forecasts for the 11 flights that have observed LLJs, including F46 and F49. Overall, both ERA5 analyses and short-term forecasts correctly captures the intensities of the LLJs in most of the flights. Still, as for flights F46 and F49, ERA5 underestimates on average (thick black lines) the maximum wind speed by 3 $\mathrm{m.s^{-1}}$ close to the surface and by 1.5 $\mathrm{m.s^{-1}}$ between 900 hPa and 700 hPa. The bias can go up to 6 $\mathrm{m.s^{-1}}$ for some specific flights, especially close to the surface. Cross sections of horizontal wind speed for individual flights show that this underestimation near the surface is related

https://doi.org/10.5194/egusphere-2026-3987
Preprint. Discussion started: 28 July 2026

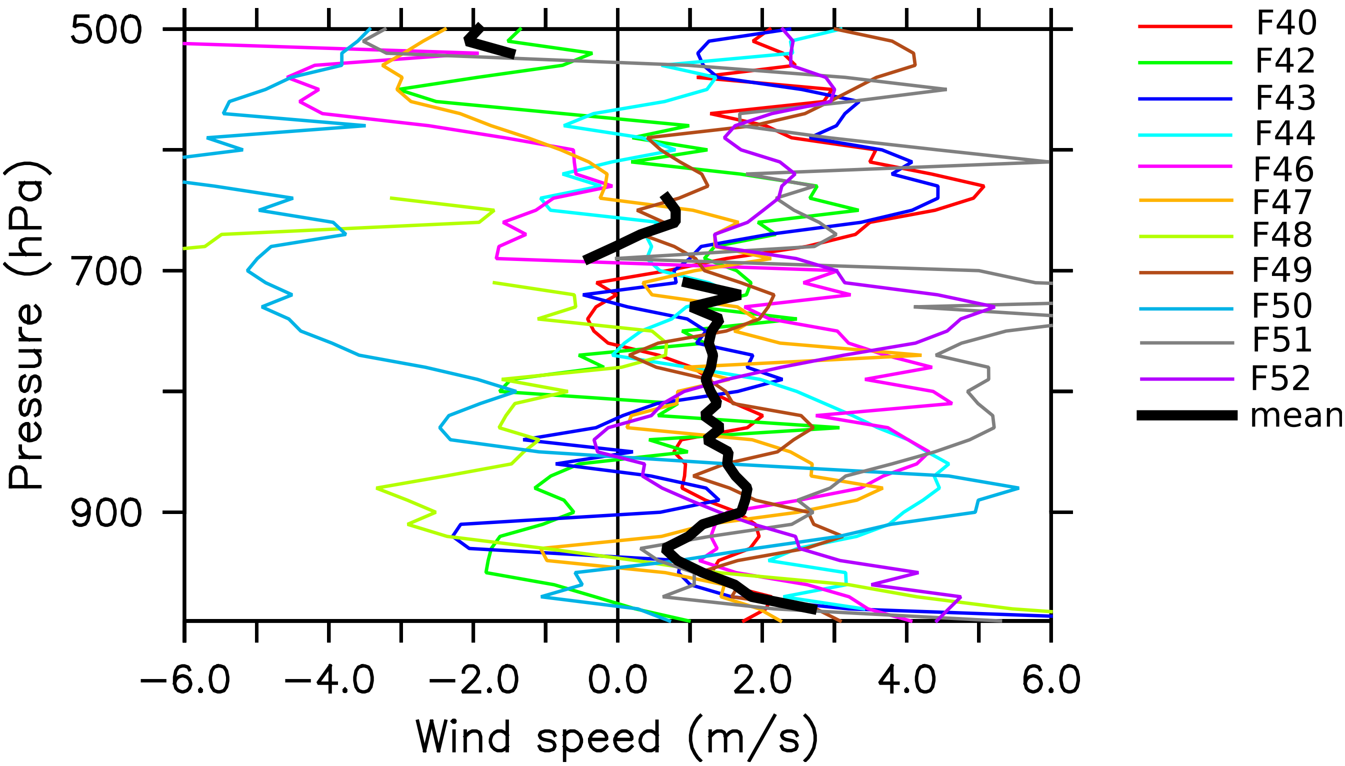

Figure 4. Difference in maximum wind speed between RASTA measurements and ERA5 forecasts (nearest grid point) at each vertical level. The mean difference is shown in bold black line. ERA5 short-term forecasts are selected such that their initialisation is the closest to the flight time, i.e. between 1h and 12h before the flight. The trajectories for each flight are shown in Rivière et al. (2024).

to a higher peak altitude of the LLJ in ERA5 than in the observations (figure S1). Similar conclusions can be drawn for ERA5 analyses (figure S2 in the supplement). To conclude, both ERA5 reanalyse and short-term forecasts slightly underestimate the intensity of the LLJs and position them at an altitude a bit too high compared to the radar observations despite some case-to-case variability.

4 Analysis of the intense northeasterly jet of cyclone AC3

4.1 Baroclinic phase

The general structure of the cyclone at 14:00 UTC on 16 August 2022 when the cyclone has still a baroclinic structure and well-defined fronts is shown in Fig. 5. It exhibits an asymmetric structure with a well-defined zonally-extended warm front centred around 76° N and 10° E. A strong westward jet has developed on the cold sector of the warm front, with wind speed reaching 25 $\mathrm{m.s^{-1}}$, which can thus be identified as the CCB. The warm front is well located by the narrow band of high low-level PV southward of the CCB jet (Fig. 5a). Both the PV band and the isentropes of the warm front northward tilt with height

https://doi.org/10.5194/egusphere-2026-3987
Preprint. Discussion started: 28 July 2026

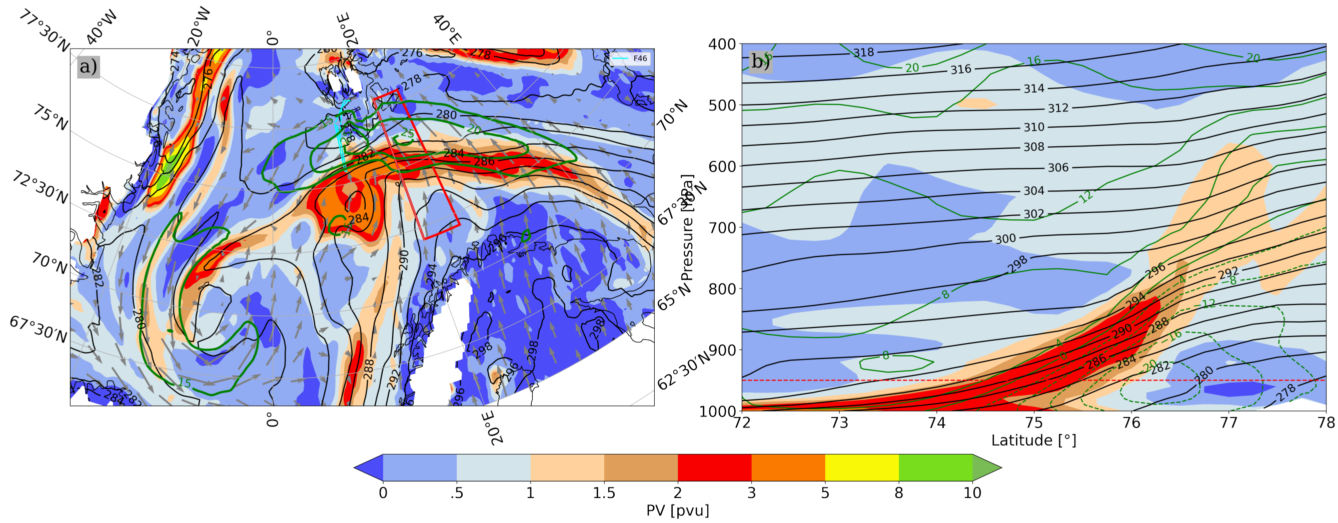

Figure 5. General structure of cyclone AC3 during its baroclinic phase at 14:00 UTC on 16 August 2022. *(a)* PV (shading), temperature (black contours), wind (green contours when above 15 $\mathrm{m.s-1}$) and its directions (grey arrows) at 950 hPa. **(b)** Cross sections of the zonal means between 15° E and 25° E of the same variables, except that only the zonal wind is shown in green contours with negative values in dashed lines. The red box in panel a) is the region where the zonal mean is computed for panel b). The horizontal dashed red line in panel b) corresponds to the pressure level shown in panel a). Data are from ERA5 short-term forecasts.

from the surface up to 750 hPa approximately (Fig. 5b). The associated westward jet is right below and to the north of the PV band. It is worth noting that the high PV values extend southward below 950 hPa. The CCB extends all along the bent-back front around the low pressure centre around 15°W associated with an extension of the PV band (Fig. 5a).

In order to understand how the PV band along the warm front was generated, we have traced back air parcels associated with high PV and followed which processes generated this PV. Backward trajectories have been initiated where the PV is equal or higher than 2 PVU in a box around the cyclone every 1° of longitude between -15° E and 33° E, every 0.25° of latitude between 66° N and 78° N and every 10hPa between 850 hPa and 950 hPa. Trajectories initiated not within the PV band associated with the cold front have been removed. Backward trajectories have been computed every 30 minutes during 12h. The 1402 resulting backward trajectories are shown in Fig. 6a. High PV air parcels forming the zonal band at the warm front are almost all rising across the warm front and start close to the surface (around 1000 hPa). The trajectories in the western part of the cyclone, around the low pressure centre, are also rising and follows the cyclonic motion. The trajectories initialised in the low-level patch of PV at 950 hPa at the junction between the cold and warm fronts stay approximately around 925 hPa.

By integrating Eq. (4) along all trajectories, we obtain the time evolution of the mean accumulated PV (Fig. 6a, black full line). The dashed grey line is the mean direct interpolation of PV along trajectories, showing a fair agreement with the accumulated PV. The abrupt change in PV between 06:00 and 07:00 UTC comes from the fact that the dataset at 06:00 UTC comes from the forecast initialised at 18:00 UTC on 15 August whereas the one at 07:00 belongs to the forecast at 06:00 UTC

https://doi.org/10.5194/egusphere-2026-3987
Preprint. Discussion started: 28 July 2026

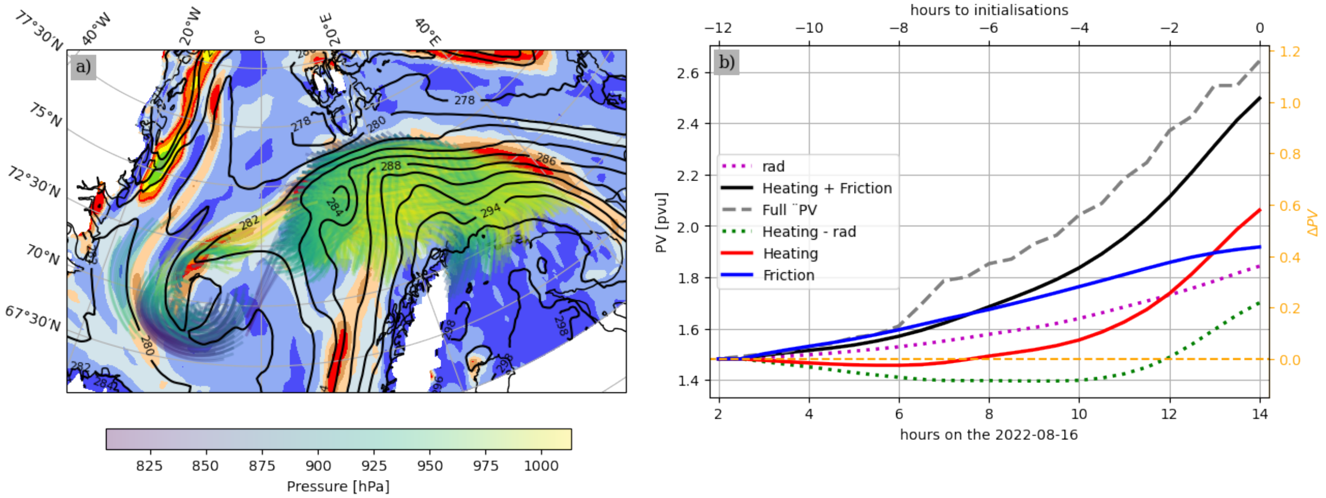

Figure 6. *(a)* 12-hour backward trajectories initiated at 2pm, 16 August 2022, where the PV is higher than 2 PVU in the warm front region. 900 hPa PV and potential temperature are shown in shading (same colorbar as Fig. 5) and black contours respectively. *(b)* Mean evolution of PV along all trajectories. The black line shows the accumulated PV obtained by integrating in time Eq. (4) from 02:00 to 14:00 on 16 August 2022. The diabatic contribution is shown in red line, and the friction contribution in blue line. The diabatic contribution is also decomposed into the generation of PV due to radiative effects (magenta dotted line) and due to the other diabatic processes (latent heating from water phase changes or heat vertical turbulent transport). The grey dashed line is the mean direct interpolation of PV along all trajectories. Data are from ERA5 short-term forecasts.

on 16 August. Except for that particular abrupt change, the slopes of the real PV (dashed line) and the accumulated PV from all the non conservatives processes (full black line) are very close to each other and shows that our PV budget is reasonably closed. During the last 12 hours, there is a substantial generation of PV, with a gain of 1 PVU. The blue and red solid lines correspond to the generation of PV due to frictional and heating processes corresponding to the first and last three terms of Eq. (4) respectively. While friction generates PV at a quite constant rate all along the time period, heating processes mostly generate PV during the last 4 hours of the trajectories. This diabatic generation of PV is mainly due to radiative effects (dotted magenta line), with a total mean gain of 0.4 PVU, while other heating sources contribute to 0.2 PVU.

To further investigate PV generation by radiative processes, Fig. 7a shows the heating rate at 950 hPa at the time of the maximum generation of PV due to long-wave radiation, i.e. at 13:00 UTC on 16 August. Trajectories that generate (green "plus" signs) or destroy (magenta "minus" signs) at least 1 $\mathrm{PVU.h^{-1}}$ through long-wave radiative processes at this time and located between 940 and 960 hPa are shown. PV generation by short-wave radiative processes are negligible compared to long-wave ones (not shown). Most of those trajectories are located at the crossing point between warm and cold fronts, where there is a strong long-wave radiative cooling. Figure 7b shows that the radiative cooling occurs just above low-level clouds south of the warm front, i.e. boundary layer clouds, and most of the trajectories that generate PV through this process are located just above the cooling region. Investigation of liquid and ice water contents reveal that those clouds are mostly liquid (not shown).

https://doi.org/10.5194/egusphere-2026-3987
Preprint. Discussion started: 28 July 2026

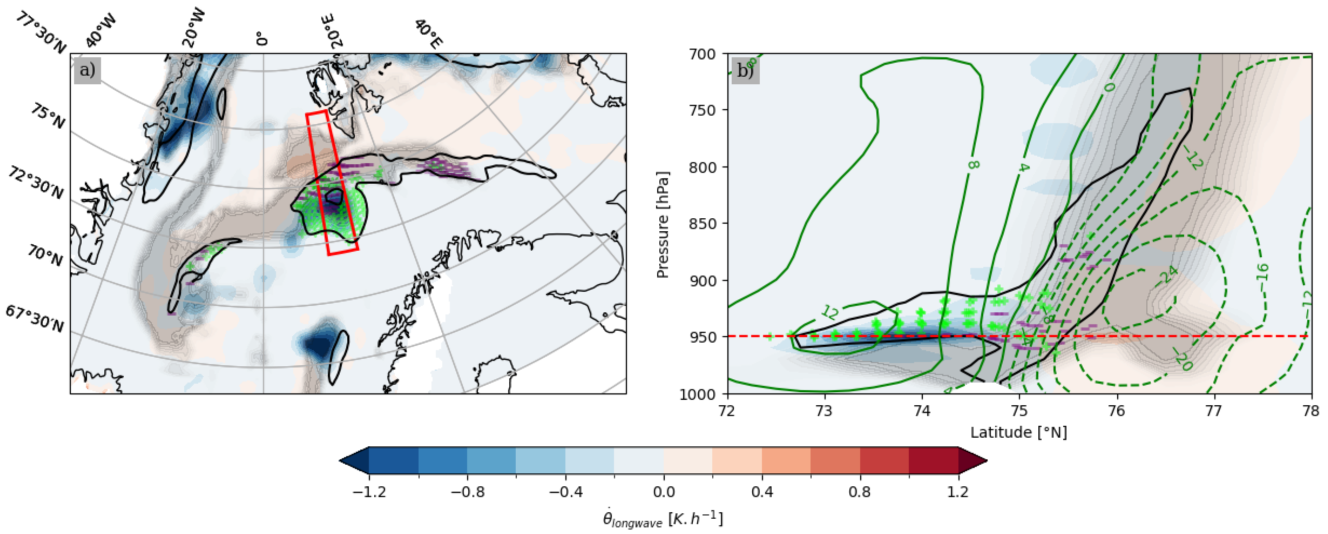

Figure 7. Potential temperature tendency due to longwave radiative heating / cooling and locations of trajectories that generate or destroy PV through this process. They are snapshots at 13:00 UTC on 16 August 2022, time of the largest mean production of PV due to this process. Only trajectories that generate (green '+') or destroy (magenta '-') at least 0.1 $\mathrm{PVU.h}^{-1}$ through long-wave radiative processes at this time are selected. *(a)* At 950 hPa level. Only trajectories located between 940 and 960 hPa at this time are shown. Black contours corresponds to the 2-PVU isoline. *(b)* Zonal mean done on the red box in left figure with the zonal mean of the horizontal wind in green contours. Only trajectories inside the box are shown, all along the vertical. The horizontal dashed red line corresponds at the vertical level plotted in panel a). Data are from ERA5 short-term forecasts.

The term $-g(\zeta+f)\frac{\partial\dot{\theta}}{\partial p}$ in Eq. (4) is then strongly positive in this region and mostly explains the PV generation there. A few trajectories that destroy PV through long-wave radiative effects are located inside the PV band above a slight warming at the clouds base. In this region, the term $\frac{\partial\dot{\theta}}{\partial p}$ is positive and thus the term $-g(\zeta+f)\frac{\partial\dot{\theta}}{\partial p}$ now destroys PV. The second term $-g\frac{\partial u}{\partial p}\frac{\partial\dot{\theta}}{\partial y}$ has a negligible contribution as the zonal wind pressure gradient is almost null at this location. A similar conclusion holds for the $g\frac{\partial v}{\partial p}\frac{\partial\dot{\theta}}{\partial x}$ term.

Other diabatic processes including latent heating and vertical turbulent transport of heat (green dotted line in Fig. 6b) tend to slightly destroy PV at the beginning of the trajectories and then create on average 0.2 PVU when reaching the warm front. Figure 8 is similar to Fig. 7 but for all the diabatic heating excluding radiative processes. The chosen time is 12:30 UTC on 16 August when the non-radiative diabatic mean generation of PV is maximum (see slope of dotted green curve in Fig. 6). Most of the trajectories are located at the warm front and below a strong heating, where the vertical heating gradient is the highest. This heating is associated with a deep frontal nimbostratus cloud with a large cloud fraction and high cloud water contents (not shown), and is likely mainly due to the release of latent heat from condensation. Indeed, air parcels rise at the warm front and their humidity condensates when rising such that latent heat is released. As the heating pressure gradient is negative, the first term $-g(\zeta+f)\frac{\partial\dot{\theta}}{\partial p}$ acts again to generate PV. Note that cooling below clouds to the north of the deep nimbostratus near 77° N

https://doi.org/10.5194/egusphere-2026-3987
Preprint. Discussion started: 28 July 2026

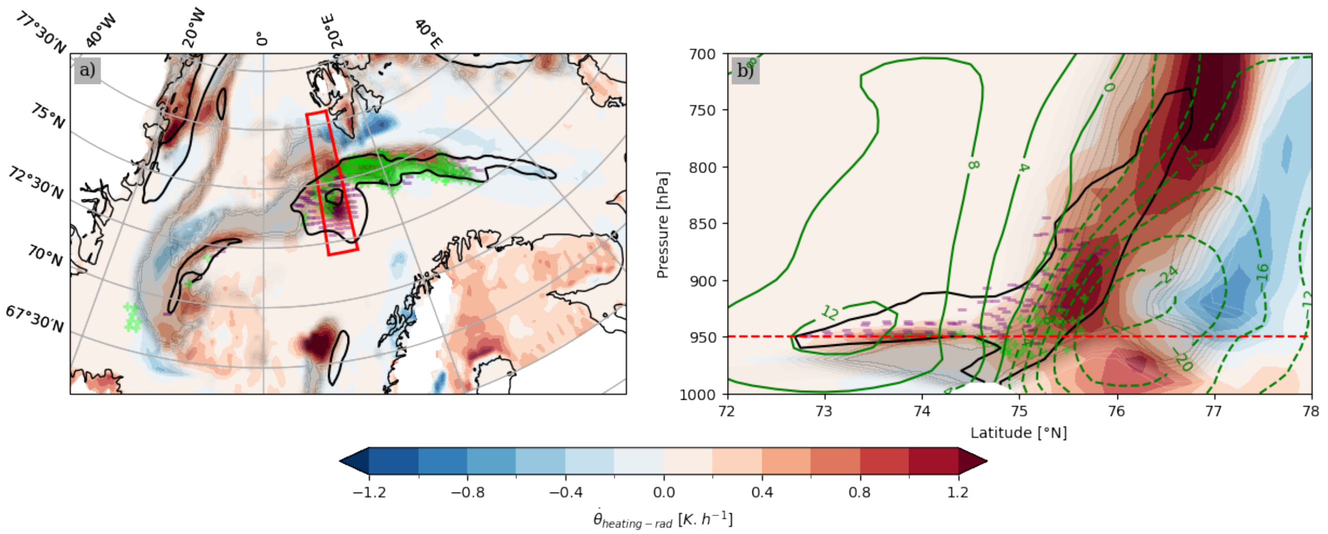

Figure 8. Similar to Fig. 7 for the diabatic heating, excluding the contribution from radiative processes, at 12:30 UTC on 16 August 2022, when the mean generation of PV due to those processes has a local maxima.

can be associated with precipitation that evaporate and is just above a PV minima in Fig. 5b. A similar PV budget performed on this region where the PV is below 1 pvu shows that this cooling is the main process destructing PV (figure S4), showing the importance of evaporation on the creation of the PV gradient, and thus the low-level jet. The boundary layer clouds are now associated with a non-radiative heating, likely due to the release of latent heat when condensing, and tend now to reduce PV.

The generation of PV due to the zonal friction depends on the meridional and vertical gradients of F_x and F_y and potential temperature. Figure 9 shows the zonal wind tendency F_x and the potential temperature at the time of the largest frictional generation of PV, along with trajectories that generate PV through this process. The criterion on trajectories is selected based on the total frictional PV generation, not only that due to F_x but also that to F_y. However, as the CCB is mainly zonal, the term F_x and its gradient are strong compared to F_y and its gradient in Eq. (4) thus the PV generation due to meridional friction is weak compared to the zonal one. At the time of maximum frictional generation of PV, at 10:00 UTC on 16 August 2022, plotted trajectories are located where the vertical pressure gradient of zonal friction is positive and the meridional gradient of potential temperature is negative such that the term $-g\frac{\partial F_x}{\partial p}\frac{\partial \theta}{\partial y}$ in Eq. (4) is positive, generating PV. This shows that baroclinicity plays a major part in the frictional generation of PV during this phase of the cyclone, as this term is proportional to the potential temperature horizontal gradient. Further analysis reveals that this term generates an average of 1 PVU, while the Ekman tendency term of PV i.e $-g(\frac{\partial F_y}{\partial x} - \frac{\partial F_x}{\partial y})\frac{\partial \theta}{\partial p}$ destroys 0.6 PVU on average, resulting on the generation of 0.4 PVU by the friction. We can see for instance a destructive region around 12° E (see magenta minus in Fig. 9b). This destruction is explained by a strong meridional gradient of F_x and a strong vertical gradient of potential temperature leading to a strong Ekman destruction of PV, with weak vertical gradient of F_x and meridional gradient of the potential temperature leading to a small baroclinic generation of PV. The pattern of the friction maxima is explained by the drag induced by the surface. In the Integrated Forecast

https://doi.org/10.5194/egusphere-2026-3987
Preprint. Discussion started: 28 July 2026

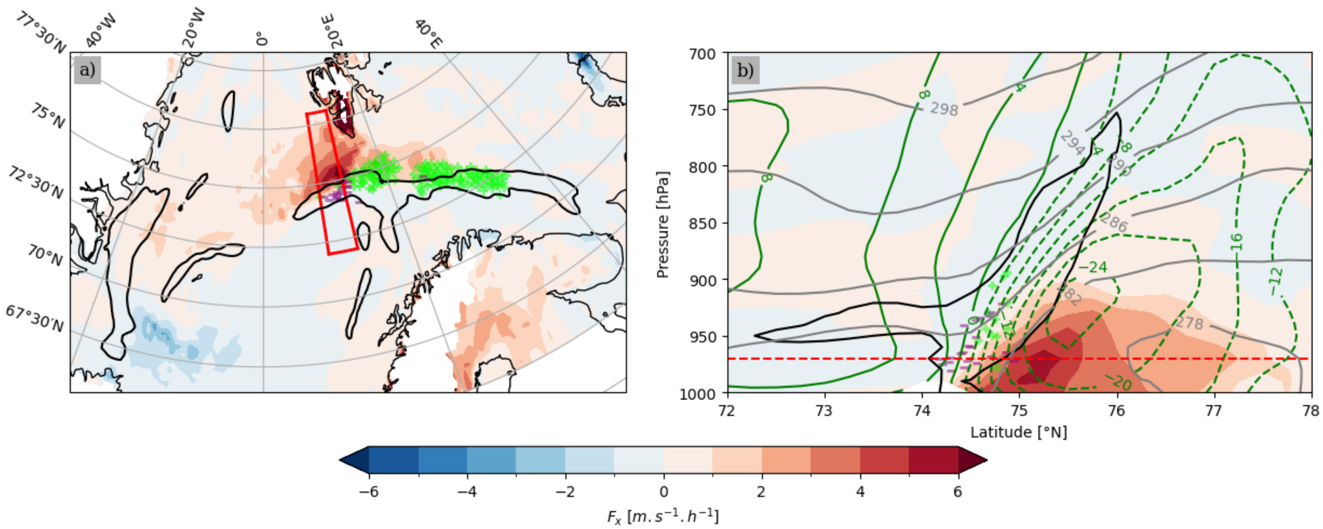

Figure 9. Similar to Fig. 7 but for the zonal wind tendency due to frictional processes, at 10:30 UTC on 16 August 2022, time of the largest mean production of PV due to this process. The grey contours are isolines of potential temperature.

System numerical model on which ERA5 is based, vertical turbulent transport of momentum is parameterised using a diffusion approach such that friction can be approximated by a turbulent diffusion term $F_x = -\frac{1}{\rho}\frac{\partial}{\partial z}(\rho u'w') \approx \frac{\partial}{\partial z}(K_m \frac{\partial u}{\partial z})$ with u the zonal wind and K_m the diffusion coefficient that depends on altitude and stability, explaining why the friction is not maximum where the jet is located but below it where the vertical wind shear is strong.

Such analysis shows that many localised fine-scale processes are at stake to create low-level PV associated with the CCB during this phase of the cyclone. Radiative cooling at the top of clouds ($\approx 40\%$ of the accumulated PV) and friction ($\approx 40\%$), due to the baroclinic structure of the cyclone during this phase, are the dominant processes generating PV on the southern side of the CCB jet, and in that sense reinforce the PV gradient and therefore the jet. Other diabatic processes generate a non-negligible amount of PV, such as latent heating released during condensation in the deep frontal nimbostratus and vertical turbulent transport ($\approx 20\%$ in the PV generation). Cooling from evaporation of precipitation at the north of the warm front destroys PV and reinforces the PV gradient as well.

4.2 Beginning of the cold-core phase

We perform the same analysis when the cyclone is at the beginning of its cold-core phase. A snapshot of its structure is shown in Fig. 10. There is almost no warm front anymore and there is still a northeasterly LLJ associated with a well-defined PV band but it is now way more extended and the winds are overall weaker (maxima of 20 $\mathrm{m.s^{-1}}$ at 900 hPa). The meridional cross section inside the red box shows that the PV band extends up to 450 hPa and tilts northward with height. The maximum of the jet is now above 800 hPa, thus further up compared to the baroclinic phase, which is consistent with the cold-core structure, that is more "upper-level" dominated. The isentropes are less tilted confirming a less pronounced front.

https://doi.org/10.5194/egusphere-2026-3987
Preprint. Discussion started: 28 July 2026

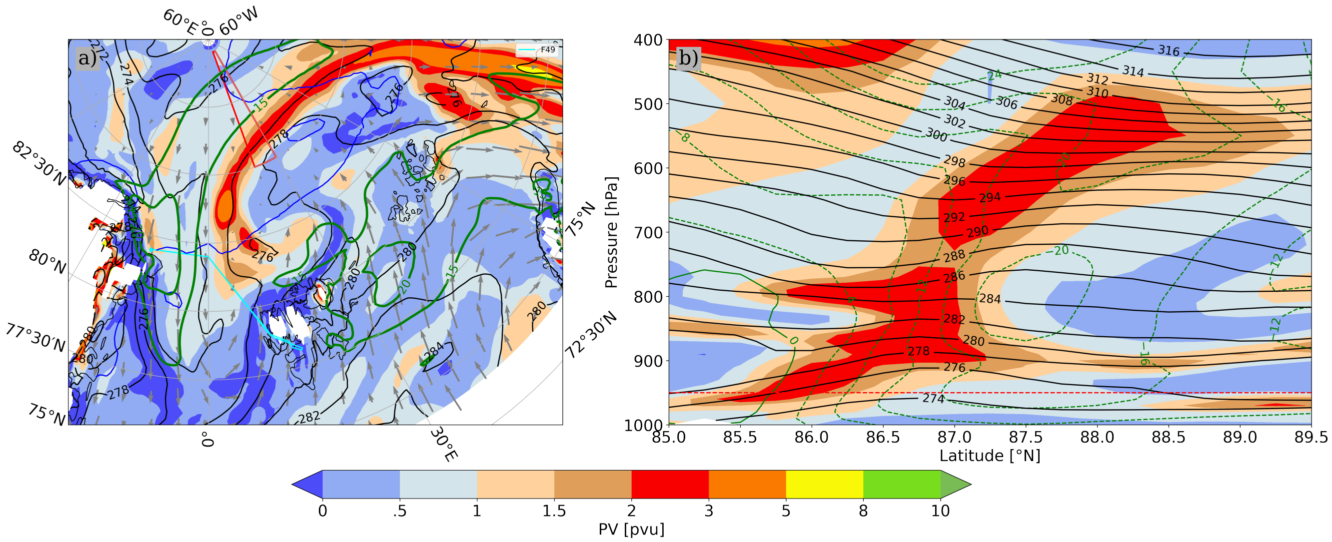

Figure 10. General structure of cyclone AC3, at the end of the core transition on the 19th of August at 2pm. *(a)* Same as Fig. 5a with the 80 % sea ice cover contour shown in blue. **(b)** Cross section of the meridional mean performed on the red box (84° N – 85° N and 30°W – 20° E), with green contours showing meridional wind.

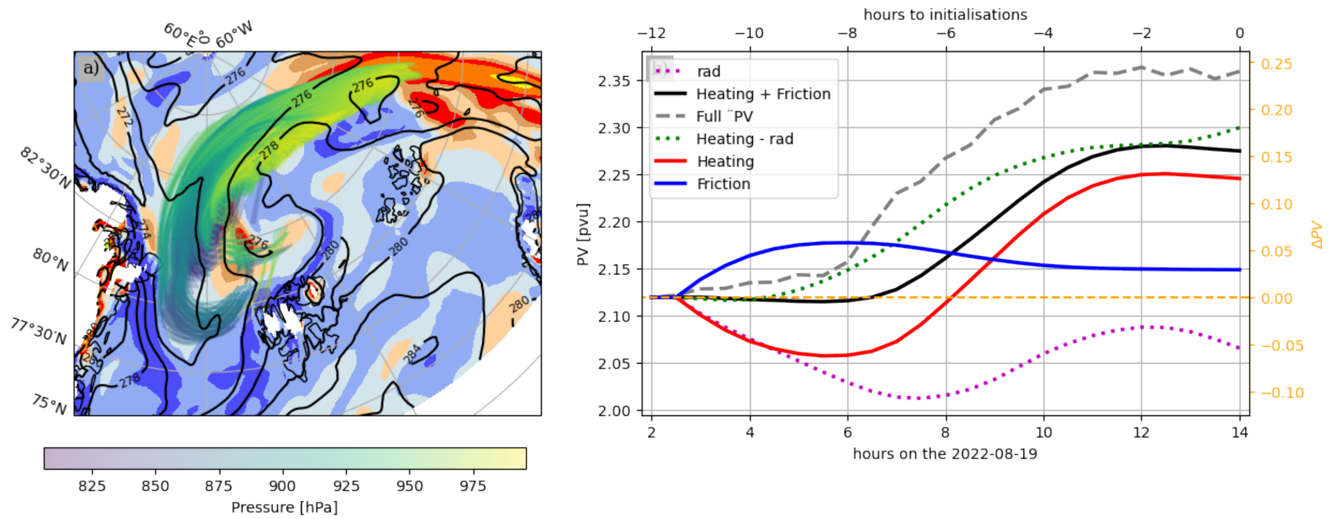

Figure 11. 12-hours backward trajectories initiated at 14:00 UTC on 19 August 2022, where the PV is higher than 2 PVU. 900 hPa PV and potential temperature are shown in shading (same colorbar as Fig. 10) and black contours respectively. The legends are the same as in Fig. 6.

Trajectories have been initialised at 14:00 UTC on 19 August in high PV regions between 10°W and 30° E every 1 degree, between 79° N and 87.78° N every 0.25° and between 950 hPa and 850 hPa every 10 hPa. The 2524 resulting trajectories are shown in Fig. 11a and the mean accumulated PV by the different processes along all trajectories are plotted in Fig. 11b.

https://doi.org/10.5194/egusphere-2026-3987
Preprint. Discussion started: 28 July 2026

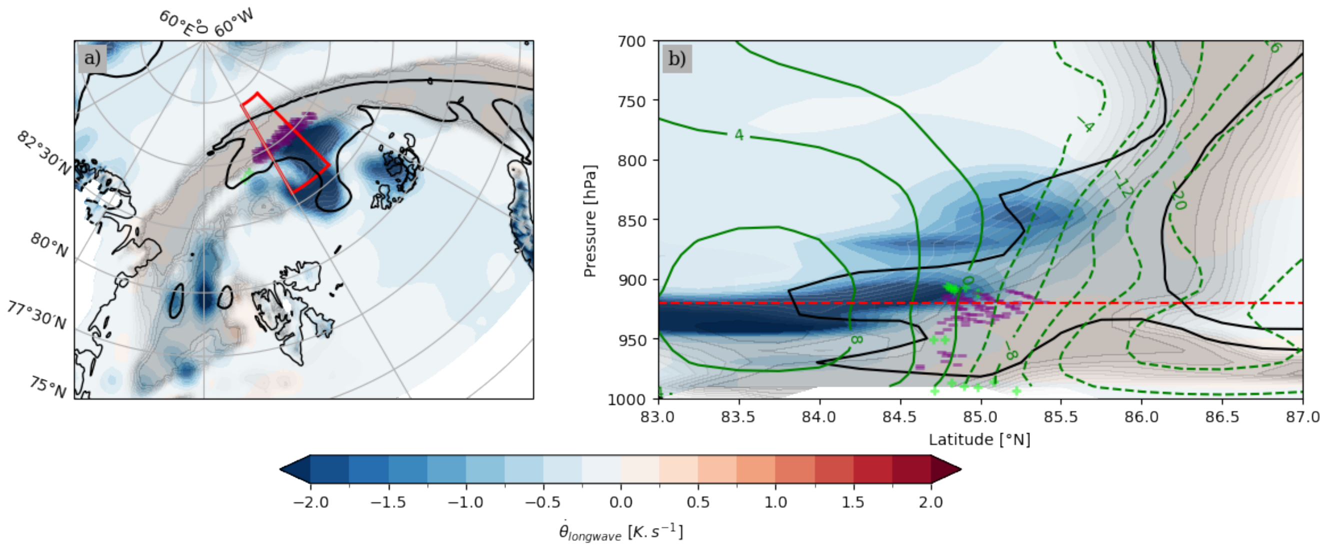

Figure 12. Map of potential temperature tendencies due to longwave radiation and location of trajectories at the time of maximum radiative heating mean destruction of PV, at 04:00 UTC on 19 August 2022. The zonal mean in panel (b) is performed between 30° E and 45° E.

The mean gain of PV is only 0.15 PVU (compared to 1 PVU during the other phase). The most prominent difference with the former phase is that the net friction PV accumulation is now almost null (0.05 PVU). This can be interpreted following Cooper et al. (1992) who have shown that the frictional generation of PV in the boundary layer is proportional to $-\boldsymbol{v_s}.\boldsymbol{v_t}$, with $\boldsymbol{v_s}$ the surface wind and $\boldsymbol{v_t}$ the thermal wind. During the baroclinic phase, the strong warm front is associated with a strong eastward thermal wind but the surface winds are westward. The thermal and surface winds are thus in opposite directions, thus there is a frictional generation of PV. However, during the cold-core phase, they are in the same direction, leading to a destruction of PV, consistent with Croad et al. (2023a). The generation of PV through non-radiative heating processes is of the same order of magnitude as in the first phase (0.2 PVU). In sharp contrast with the previous phase, radiative processes now slightly destroy PV (-0.05 PVU) on average.

Figure 12 shows how PV is generated or destroyed by long-wave radiative effects in the same way as Fig. 7 but for this phase, at 04:00 UTC on 19 August 2022 (strong average destruction of PV through radiative effects). As in the previous phase, the PV generation by short-wave radiative processes are negligible compared to long-wave ones (not shown). Investigation of liquid and ice water contents reveal that those clouds are mostly mixed-phase (not shown). The top of the clouds are higher in altitude thus the associated radiative cooling too. Below the clouds, we can point out a weak heating from long-wave absorption of the clouds. Here, the trajectories are below the cooling and above the weak heating, thus the term $-g(\zeta+f)\frac{\partial\dot{\theta}}{\partial p}$ is now destroying PV. Comparison between the baroclinic phase and cold-core phase shows that radiative cooling covers a larger area and extends more above the PV band during the latter stage than the former (compare Fig. 7 and 12) such that PV is more likely to be destroyed when air parcels reach the PV band during the latter stage.

https://doi.org/10.5194/egusphere-2026-3987
Preprint. Discussion started: 28 July 2026

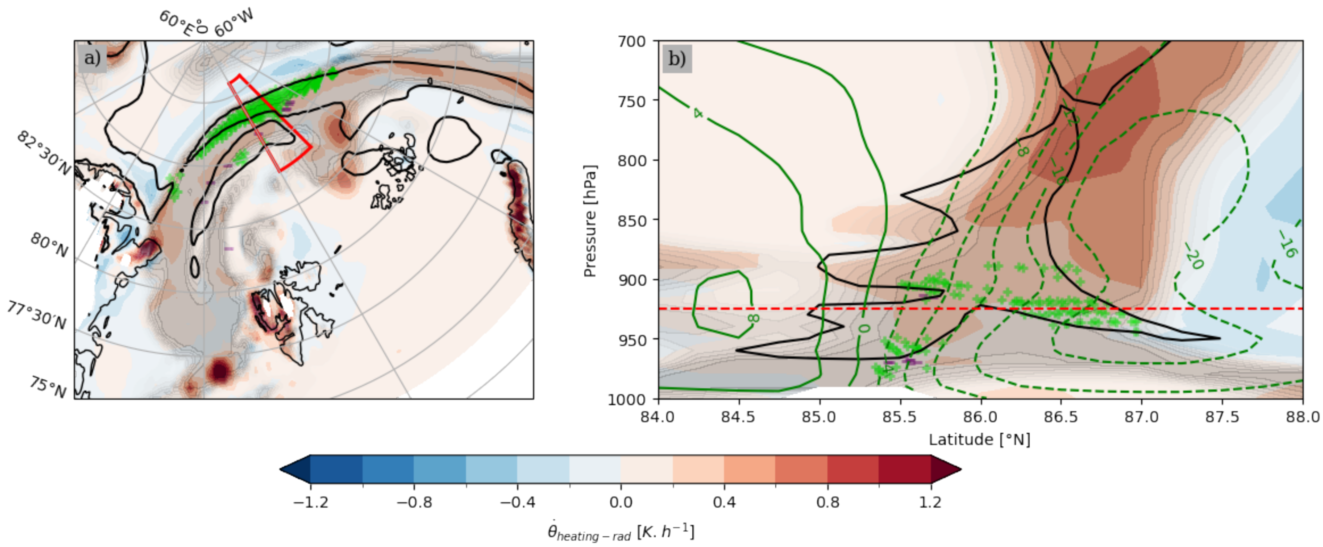

Figure 13. Map of potential temperature tendencies due to non radiative processes - mainly latent heating release and vertical turbulent heat transport - and locations of trajectories at the time of maximum non-radiative heating mean generation of PV, at 04:00 UTC on 19 August 2022 for AC3B cyclone. The zonal mean is performed between 15° E and 45° E (panel b).

The mechanism that generates PV through non-radiative heating is similar to that in the previous phase as we can see in Fig. 13. There is still a heating maximum associated with a deep nimbostratus at the PV band, though less intense than in the previous phase. The projected trajectories that generate PV are all below this heating.

The weak generation of PV by friction is mainly due by the baroclinic contribution along the warm front (around 0.06 PVU), which is partly compensated by the Ekman destruction of PV (around - 0.03 PVU), as in the previous phase. As shown in Fig. S3, this reduction of frictional generation of PV is due to the fact that the horizontal gradients of temperature has decreased in comparison with vertical gradients and the frictional baroclinic generation of PV becomes less dominant in comparison with the frictional Ekman destruction of PV. Moreover, the amplitude of the drag $|\boldsymbol{F}|$, and thus its gradients, is largely reduced because the jet is now more upper-level and interacts less with the surface, decreasing even more the generation of PV.

5 Synthesis and Discussion

In this study, we have first investigated the representation of low-level jets (LLJs) in summertime Arctic cyclones using ERA5 reanalysis products and radar observations from the THINICE campaign. Radar observations show that ERA5 short-term forecasts correctly reproduce the structure of those LLJs rather well but still underestimate their maximum intensity close to the surface. Those discrepancies might come from how sub-scale nonconservative processes are modelled inside the model, which is why it is important to understand the interactions between them and the LLJs. Using a backward Lagrangian trajectories

https://doi.org/10.5194/egusphere-2026-3987
Preprint. Discussion started: 28 July 2026

algorithm and the PV framework, we studied how those fine-scale processes affected the PV band associated with the LLJ during the transition of a well observed cyclone from a baroclinic structure to an axisymmetric cold-core structure.

Figure 14 shows a synthesis of our results by plotting the total accumulated PV along all the 12h-trajectories generated by the different processes during the baroclinic and cold-core phases. Illustrations of how the different processes generate PV in the baroclinic phase are shown in Fig. 15. The results can be summarised as follows:

- Nonconservative processes efficiently generate low-level PV along the high PV band associated with the northeasterly low-level jet during the baroclinic phase but produce much less PV during the cold-core phase (see Figs. 14g,h).

- One main difference between the two phases is that there is almost no accumulation of PV by friction at all lower levels during the cold-core phase (Fig. 14b), while there is an important frictional PV generation during the baroclinic phase on the eastern part of the warm front at most levels (Fig. 14a). Figure 15c illustrates how friction generates PV during the baroclinic region. From Eq. (4), the vectors $\nabla \times \boldsymbol{F}$ and $\boldsymbol{\nabla}\theta$ need to be co-linear to generate PV: there is then a strong generation of PV above the friction maxima and a small destruction region close to the ground south of the maxima. In the cold-core case, isentropes would be less tilted, and the amplitude of the friction would be less intense and closer to the ground, leading to a reduced effect of friction on PV. The counter-intuitive effect of the friction generating PV in a region of high PV and hence reinforcing the jet can be explained as follows. The scalar product between $\boldsymbol{\nabla} \times \boldsymbol{\zeta_{abs}}$ and $\boldsymbol{\nabla}\theta$ is positive because of the colinearity of the vertical components but the scalar product between $\boldsymbol{\nabla} \times \boldsymbol{F}$ and $\boldsymbol{\nabla}\theta$ is also positive because of the colinearity of the horizontal components. Thus both scalar products $(\boldsymbol{\nabla} \times \boldsymbol{\zeta_{abs}}) \cdot \boldsymbol{\nabla}\theta$ and $(\boldsymbol{\nabla} \times \boldsymbol{F}) \cdot \boldsymbol{\nabla}\theta$ can be positive even though $\boldsymbol{u}$ and $\boldsymbol{F}$ point in the opposite direction.

- The effect of the shallow clouds during the baroclinic phase is such that there is an accumulation of PV through radiative processes (Fig. 14c) despite the PV destruction through non-radiative diabatic processes close to the ground in the region where the warm front and the cold front meet (Fig. 14e). The net effect is to generate PV. The effects of those boundary layer clouds on the PV generation are illustrated on Figs. 15a,b. From Eq. (4), the vectors $\nabla \times \zeta_{abs}$ and $\boldsymbol{\nabla}\dot{\theta}$ need to be co-linear to generate PV, leading to a generation of PV by radiative processes above the boundary layer clouds and to a destruction of PV by other non radiative diabatic processes above the clouds. During the cold-core phase similar tendencies are observed near the ground, which might suggest the presence of similar shallow clouds. But during that phase, radiative cooling extends further up to 800 hPa above the lower part of the PV band such that air masses in the PV band undergo PV destruction via radiative processes in most areas (Fig. 14d).

- Diabatic non-radiative effects substantially accumulate PV all along the warm front at all levels during the baroclinic phase while those processes have almost no effect between 900 hPa and 950 hPa during the cold-core phase (see Fig. 14e,f). Above 900 hPa, non radiative heating locally generates or destroys PV but in average generation is more important than destruction. Most of this PV generation comes from the region below the latent heating by the condensation of the deep frontal nimbostratus, as it is illustrated in Fig. 15a. This mechanism is similar in both phases, except that isentropes are less tilted in the cold-core phase and the latent heating is weaker and more in altitude than in the baroclinic

https://doi.org/10.5194/egusphere-2026-3987
Preprint. Discussion started: 28 July 2026

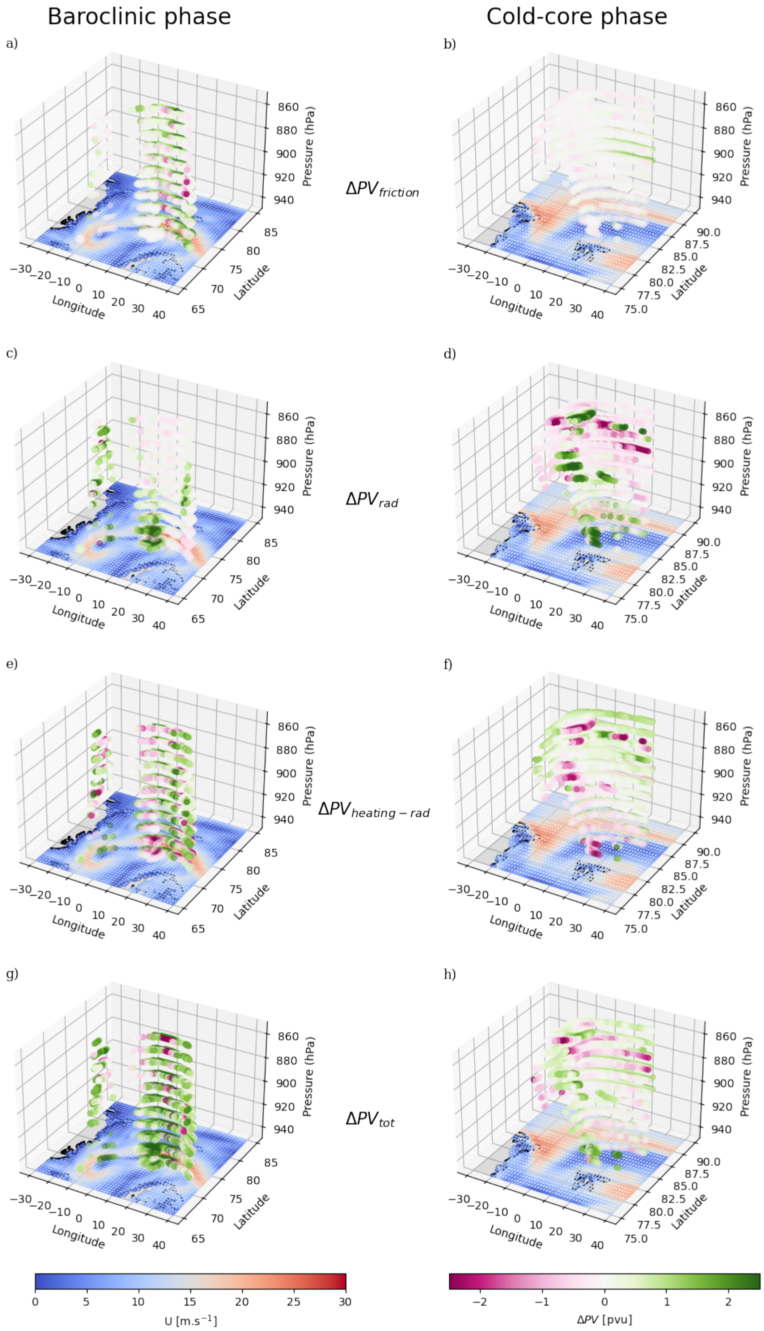

Figure 14. Accumulated PV along each 12h-trajectory at their initialisation times for the different processes, i.e. friction, radiative processes and non radiative diabatic processes, and for the different cyclone phases. Only points with a PV above 2 PVU are shown, every 10 hPa between 950 hPa and 850 hPa. Wind intensity at 950 hPa level is also shown. Data are from ERA5 short-term forecasts.

https://doi.org/10.5194/egusphere-2026-3987
Preprint. Discussion started: 28 July 2026

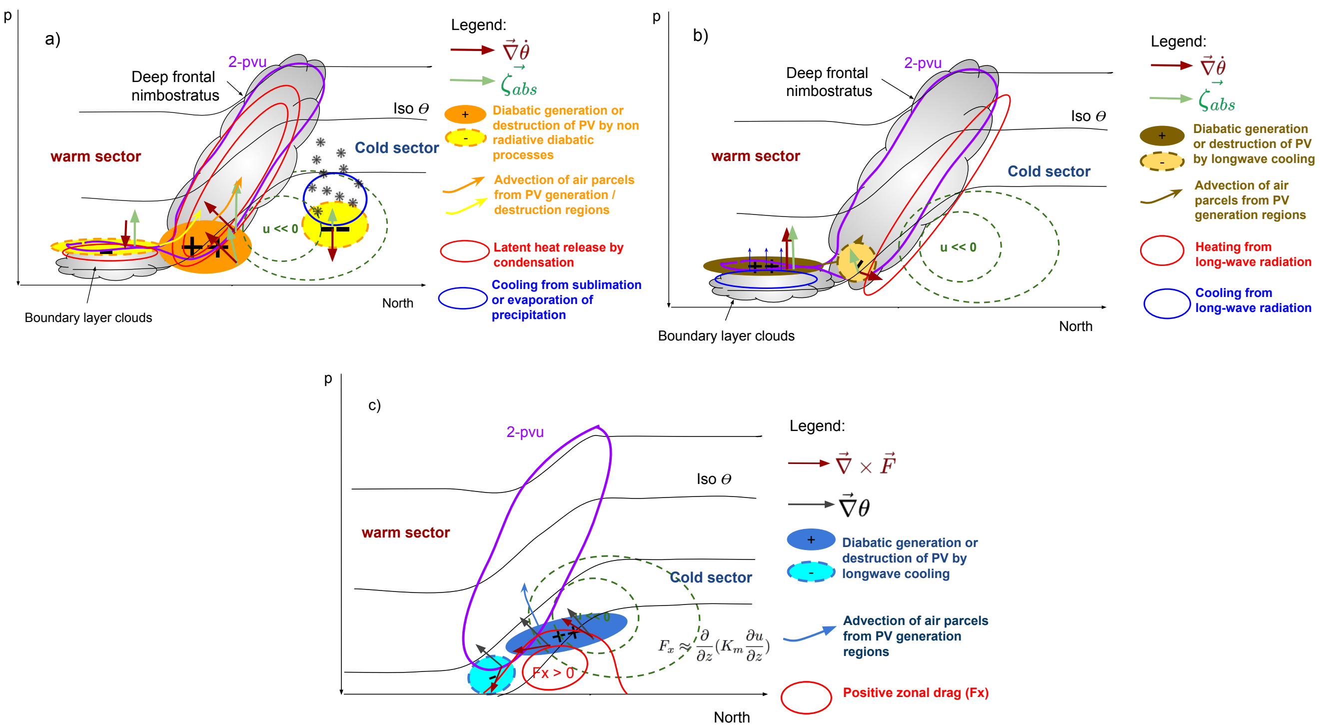

Figure 15. Schematics of how radiative diabatic processes (a), other diabatic processes (b) and frictional processes (c) generate PV at the warm front during the baroclinic phase. According to Eq. (4), there is generation of PV by friction when $\nabla \times \boldsymbol{F}.\nabla\theta > 0$ and there is diabatic generation of PV when $\boldsymbol{\zeta_a}.\nabla\dot{\theta} = (\nabla \times \boldsymbol{u} + \boldsymbol{f_c}).\nabla\dot{\theta} > 0$.

phase. Moreover, those processes tend to increase the PV gradient, and thus the jet, by destroying PV below the cooling associated with sublimation or evaporation of precipitation in the cold sector.

Let us now discuss the results at the light of the existing literature. The frictional effects are consistent with what has been observed in other case studies in Croad et al. (2023a) and statistically in Besson et al. (2026b). Friction generates a lot of PV when the cyclone is in its baroclinic phase and has a warm core while it has almost no effect on the PV when the cyclone reaches a cold-core structure after the baroclinic phase. In our case, we do observe the PV generation during the baroclinic phase and almost no PV tendency during the cold-core phase.

We have shown that radiative processes play a primary role in generating or destroying PV during cyclone AC3 in the vicinity of shallow clouds. It is worth noting that these clouds - mostly of mixed phase composition in the cold core phase - are particularly challenging to model (Forbes and Ahlgrimm, 2014; Vignon et al., 2026; Schulte et al., 2026; Raillard et al., 2026) - which questions to what extent the structure of the LLJ depends on modelling choices and cloud parameterisations.

The results of cyclone AC3 during its baroclinic phase can be also compared to those of Attinger et al. (2021) who studied 144 Northern Hemisphere extratropical - mainly mid-latitude - cyclones during the warm season. They found that turbulent

https://doi.org/10.5194/egusphere-2026-3987
Preprint. Discussion started: 28 July 2026

mixing of momentum and condensation are the main processes generating PV at the warm front, which is consistent with what we observe. Similarly, they found that condensation is the main contribution to the generation of PV around the cyclone center. The latter result differs from what we observe in our case, as long-wave radiative processes is the main process generating PV near the cyclone center in that region during the baroclinic phase.

This work shows how the same fine-scale processes can impact differently the LLJs of one summertime Arctic cyclone depending on its structure and phase. Future avenues may explore to what extent the structure of the low-level jets depends on the subgrid parameterisations of clouds and turbulence in atmospheric models and to what extent the uncertainties in jets representation can be attributed to uncertainties in parameterisations' calibration.

Code availability. The version of the algorithm used to compute the backward Lagrangian trajectories named Lagrantraj is available here: https://github.com/NicolasChiabrando/LagranTraj.git. The python routine used to interpolate data from model levels to pressure level can be found here https://github.com/lguez/Ml2pl.git. The python routines used to preprocess the data adn make the plots are available here : https://github.com/NicolasChiabrando/Low-level-jets-of-Arctic-cyclone-AC3.git.

Data availability. THINICE data are freely distributed on the campaign website https://ralithinice.aeris-data.fr/. ERA5 data and ERA5 short-term forecasts are accessible via the climate data store (https://doi.org/10.24381/cds.bd0915c6, Hersbach et al. (2020)).

Acknowledgements. This research has been funded by the CYCLONICE and DEMONIAC projects of the CNRS-INSU LEFE program. Airborne wind data were obtained using the aircraft managed by SAFIRE, the French facility for airborne research, an infrastructure of the French National Center for Scientific Research (CNRS), Météo-France and the French National Center for Space Studies (CNES). The processing of airborne radar data have been supported by the EECLAT project, funded by CNES.

This study was conducted using the ESPRI (Ensemble de Services Pour la Recherche l'IPSL) computing and data center (https://mesocentre.ipsl.fr) which is supported by CNRS, Sorbonne Université, Ecole Polytechnique, and CNES and through national and international grants. This study was initiated by Mathieu Barbe during his master 1 thesis.

https://doi.org/10.5194/egusphere-2026-3987
Preprint. Discussion started: 28 July 2026

References

Adamson, D. S., Belcher, S. E., Hoskins, B. J., and Plant, R. S.: Boundary-layer friction in midlatitude cyclones, Quarterly Journal of the Royal Meteorological Society, 132, 101–124, https://doi.org/https://doi.org/10.1256/qj.04.145, 2006.

Attinger, R., Spreitzer, E., Boettcher, M., Forbes, R., Wernli, H., and Joos, H.: Quantifying the role of individual diabatic processes for the formation of PV anomalies in a North Pacific cyclone, Quarterly Journal of the Royal Meteorological Society, 145, 2454–2476, https://doi.org/https://doi.org/10.1002/qj.3573, 2019.

Attinger, R., Spreitzer, E., Boettcher, M., Wernli, H., and Joos, H.: Systematic assessment of the diabatic processes that modify low-level potential vorticity in extratropical cyclones, Weather and Climate Dynamics, 2, 1073–1091, https://doi.org/10.5194/wcd-2-1073-2021, 2021.

Besson, M., Rivière, G., and Fromang, S.: A cyclone phase space dedicated to extratropical cyclones, Weather and Climate Dynamics, 7, 805–823, https://doi.org/10.5194/wcd-7-805-2026, 2026a.

Besson, M., Rivière, G., and Fromang, S.: The life cycles of long summertime Arctic cyclones, Weather and Climate Dynamics, p. To be submitted, 2026b.

Carlson, T.: Airflow through midlatitude cyclones and the comma cloud pattern, Mon. Weather Rev., pp. 1498–1509, 1980.

Cooper, I. M., Thorpe, A. J., and Bishop, C. H.: The Role of Diffusive Effects On Potential Vorticity In Fronts, Quarterly Journal of the Royal Meteorological Society, 118, 629–647, https://doi.org/https://doi.org/10.1002/qj.49711850603, 1992.

Croad, H. L., Methven, J., Harvey, B., Keeley, S. P. E., and Volonté, A.: The role of boundary layer processes in summer-time Arctic cyclones, Weather and Climate Dynamics, 4, 617–638, https://doi.org/10.5194/wcd-4-617-2023, 2023a.

Croad, H. L., Methven, J., Harvey, B., Keeley, S. P. E., Volonté, A., and Hodges, K. I.: A Climatology of Summer-Time Arctic Cyclones Using a Modified Phase Space, Geophysical Research Letters, 50, e2023GL105 993, https://doi.org/https://doi.org/10.1029/2023GL105993, e2023GL105993 2023GL105993, 2023b.

Delanoë, J., Protat, A., Jourdan, O., Pelon, J., Papazzoni, M., Dupuy, R., Gayet, J.-F., and Jouan, C.: Comparison of Airborne In Situ, Airborne Radar–Lidar, and Spaceborne Radar–Lidar Retrievals of Polar Ice Cloud Properties Sampled during the POLARCAT Campaign, Journal of Atmospheric and Oceanic Technology, 30, 57 – 73, https://doi.org/10.1175/JTECH-D-11-00200.1, 2013.

Deshmukh, V., Rivière, G., Fromang, S., and Saint-Lu, M.: How Does a Dry General Circulation Model Represent Atmospheric Blocking?, Journal of the Atmospheric Sciences, 82, 283 – 300, https://doi.org/10.1175/JAS-D-24-0048.1, 2025.

ECMWF: IFS Documentation CY50R1 - Part 4: Physical Processes, ECMWF, https://doi.org/10.21957/49928f2338, 2026.

Ertell, H.: Ein neuer hydrodynamischer Erhaltungssatz, Naturwissenschaften, 30, 543–544, https://doi.org/10.1007/BF01475602, 1942.

Finocchio, P. M., Doyle, J. D., and Stern, D. P.: Accelerated Sea Ice Loss from Late Summer Cyclones in the New Arctic, Journal of Climate, 35, 7751 – 7769, https://doi.org/10.1175/JCLI-D-22-0315.1, 2022.

Forbes, R. M. and Ahlgrimm, M.: On the Representation of High-Latitude Boundary Layer Mixed-Phase Cloud in the ECMWF Global Model, Monthly Weather Review, 142, 3425 – 3445, https://doi.org/10.1175/MWR-D-13-00325.1, 2014.

Gray, S. L., Hodges, K. I., Vautrey, J. L., and Methven, J.: The role of tropopause polar vortices in the intensification of summer Arctic cyclones, Weather and Climate Dynamics, 2, 1303–1324, https://doi.org/10.5194/wcd-2-1303-2021, 2021.

Hersbach, H., Bell, B., Berrisford, P., Hirahara, S., Horányi, A., Muñoz-Sabater, J., Nicolas, J., Peubey, C., Radu, R., Schepers, D., Simmons, A., Soci, C., Abdalla, S., Abellan, X., Balsamo, G., Bechtold, P., Biavati, G., Bidlot, J., Bonavita, M., De Chiara, G., Dahlgren, P., Dee, D., Diamantakis, M., Dragani, R., Flemming, J., Forbes, R., Fuentes, M., Geer, A., Haimberger, L., Healy, S., Hogan, R. J., Hólm, E., Janisková, M., Keeley, S., Laloyaux, P., Lopez, P., Lupu, C., Radnoti, G., de Rosnay, P., Rozum, I., Vamborg, F., Villaume, S., and Thépaut, J.-N.: The ERA5 global reanalysis, Quarterly Journal of the Royal Meteorological Society, 146, 1999–2049, https://doi.org/https://doi.org/10.1002/qj.3803, 2020.

Peng, L., Zhang, X., Kim, J.-H., Cho, K.-H., Kim, B.-M., Wang, Z., and Tang, H.: Role of Intense Arctic Storm in Accelerating Summer Sea Ice Melt: An In Situ Observational Study, Geophysical Research Letters, 48, e2021GL092 714, https://doi.org/https://doi.org/10.1029/2021GL092714, e2021GL092714 2021GL092714, 2021.

Raillard, L., Vignon, E., Rivière, G., and Madeleine, J.-B.: A Turbulence-Informed Parameterization of Phase Partitioning in Stratiform Mixed-Phase Clouds for the LMDZ Model, Journal of Advances in Modeling Earth Systems, 18, e2025MS005 100, https://doi.org/https://doi.org/10.1029/2025MS005100, e2025MS005100 2025MS005100, 2026.

Rivière, G., Wimmer, M., Arbogast, P., Piriou, J.-M., Delanoë, J., Labadie, C., Cazenave, Q., and Pelon, J.: The impact of deep convection representation in a global atmospheric model on the warm conveyor belt and jet stream during NAWDEX IOP6, Weather and Climate Dynamics, 2, 1011–1031, https://doi.org/10.5194/wcd-2-1011-2021, 2021.

Rivière, G., Delanoë, J., Doyle, J. D., Methven, J., Barrell, C., Fearon, M., Gray, S., Johnson, A., Jourdan, O., Lachlan-Cope, T., Renfrew, I., Torn, R. D., Volonté, A., Weiss, A., Wimmer, M., Aubry, C., Baudoux, A., Bazile, E., Beeden, D., Bennett, M., Biernat, K., Bitz, C. M., Blanchard-Wrigglesworth, E., Bounissou, S., Bray, M., Burg, T., Burzdak, J., Businger, S., Capute, P., Caudoux, C., Cavallo, S., Cossalter, L., Cozzolino, C., Croad, H., Douet, V., Elvidge, A., Finocchio, P., Gourbeyre, C., Harvey, B., Huet, K., Hutchinson, T., Ladkin, R., Marshland, K., Martinez-Alvarado, O., Mioche, G., Pantillon, F., Paquette, C., Parsons, D. B., Persson, O., Raillard, L., Raut, J.-C., Seity, Y., Trules, J., Vignon, E., and Wang, X.: The THINICE Field Campaign: Interactions between Arctic Cyclones, Tropopause Polar Vortices, Clouds, and Sea Ice in Summer, Bulletin of the American Meteorological Society, 105, E2330 – E2354, https://doi.org/10.1175/BAMS-D-23-0143.1, 2024.

Schulte, L., Forbes, R., Magnusson, L., Schemann, V., Day, J., and Crewell, S.: Towards improving Arctic mixed-phase cloud representation in the ECMWF model using MOSAiC observations, Quarterly Journal of the Royal Meteorological Society, n/a, e70 205, https://doi.org/https://doi.org/10.1002/qj.70205, 2026.

Schultz, D. M.: Reexamining the Cold Conveyor Belt, Monthly Weather Review, 129, 2205–2225, https://doi.org/10.1175/1520-0493(2001)129<2205:RTCCB>2.0.CO;2, 2001.

Screen, J. A., Simmonds, I., and Keay, K.: Dramatic interannual changes of perennial Arctic sea ice linked to abnormal summer storm activity, Journal of Geophysical Research: Atmospheres, 116, https://doi.org/https://doi.org/10.1029/2011JD015847, 2011.

Serreze, M. C., Barrett, A. P., Stroeve, J. C., Kindig, D. N., and Holland, M. M.: The emergence of surface-based Arctic amplification, The Cryosphere, 3, 11–19, https://doi.org/10.5194/tc-3-11-2009, 2009.

Stoelinga, M. T.: A Potential Vorticity-Based Study of the Role of Diabatic Heating and Friction in a Numerically Simulated Baroclinic Cyclone, Monthly Weather Review, 124, 849 – 874, https://doi.org/10.1175/1520-0493(1996)124<0849:APVBSO>2.0.CO;2, 1996.

Stoll, P. J., Graversen, R. G., Noer, G., and Hodges, K.: An objective global climatology of polar lows based on reanalysis data, Quarterly Journal of the Royal Meteorological Society, 144, 2099–2117, https://doi.org/https://doi.org/10.1002/qj.3309, 2018.

Tanaka, H., Yamagami, A., and Takahashi, S.: The structure and behavior of the Arctic cyclone in summer analyzed by the JRA-25/JCDAS data, Polar Science, 6, 55–69, https://doi.org/https://doi.org/10.1016/j.polar.2012.03.001, special Issue: The Second International Symposium on the Arctic Research (ISAR - 2), 2012.

Vessey, A. F., Hodges, K. I., Shaffrey, L. C., and Day, J. J.: The composite development and structure of intense synoptic-scale Arctic cyclones, Weather and Climate Dynamics, 3, 1097–1112, https://doi.org/10.5194/wcd-3-1097-2022, 2022.

https://doi.org/10.5194/egusphere-2026-3987
Preprint. Discussion started: 28 July 2026

Vignon, E., Raillard, L., Borella, A., Rivière, G., and Madeleine, J.-B.: Modeling the coupled and decoupled states of polar boundary-layer mixed-phase clouds, Atmospheric Chemistry and Physics, 26, 1847–1865, https://doi.org/10.5194/acp-26-1847-2026, 2026.

Waseda, T., Nose, T., Kodaira, T., Sasmal, K., and Webb, A.: Climatic trends of extreme wave events caused by Arctic Cyclones in the western Arctic Ocean, Polar Science, 27, 100 625, https://doi.org/https://doi.org/10.1016/j.polar.2020.100625, arctic Challenge for Sustainability Project (ArCS), 2021.

Wernli, H. and Gray, S. L.: The importance of diabatic processes for the dynamics of synoptic-scale extratropical weather systems – a review, Weather and Climate Dynamics, 5, 1299–1408, https://doi.org/10.5194/wcd-5-1299-2024, 2024.

Wimmer, M., Rivière, G., Arbogast, P., Piriou, J.-M., Delanoë, J., Labadie, C., Cazenave, Q., and Pelon, J.: Diabatic processes modulating the vertical structure of the jet stream above the cold front of an extratropical cyclone: sensitivity to deep convection schemes, Weather and Climate Dynamics, 3, 863–882, https://doi.org/10.5194/wcd-3-863-2022, 2022.

Zhang, X., Walsh, J. E., Zhang, J., Bhatt, U. S., and Ikeda, M.: Climatology and Interannual Variability of Arctic Cyclone Activity: 1948–2002, Journal of Climate, 17, 2300 – 2317, https://doi.org/10.1175/1520-0442(2004)017<2300:CAIVOA>2.0.CO;2, 2004.